

Study of dynamic crack branching using intrinsic cohesive surfaces with variable initial elastic stiffness

Pablo D. Zavattieri

General Motors Research and Development Center, Warren, MI 48090

ABSTRACT

As observed by Needleman and co-workers [1], it is still not clear to what extent the initially elastic cohesive surfaces are more appropriate than the initially rigid cohesive surfaces for a given application. In this work, an analysis where the initially elastic model is approached asymptotically to the initially rigid is proposed. The purpose of this analysis is to gain more insight into the numerical mechanisms that lead to different results using different approaches. It was found that convergence is only achieved when the initial cohesive stiffness is much higher than the bulk stiffness. When a relative low value of this cohesive stiffness is chosen, crack tip speed is delayed and branching is artificially increased. GM R&D report # 9650, Aug. 2003.

Introduction

Cohesive Models have been gaining significant importance in the modeling of crack propagation in recent years. The most commonly used technique to incorporate the cohesive zone model into a finite element analysis is the discrete representation of the crack which is accomplished by introducing cohesive surfaces along inter-element boundaries. Within this framework, these cohesive interfaces can be classified into two approaches: the intrinsic potential-based law used by Xu and Needleman [2], and the extrinsic linear law developed by Camacho and Ortiz [3]. The distinction between these two approaches is associated with the way the crack initiation and evolution is modeled.

In the intrinsic approach, zero-thickness interface elements are embedded between volumetric elements from the beginning of the analysis. The tensile and shear traction in the interface elements are calculated from the constitutive cohesive law. The interface between two surfaces is intact until the interface traction reaches the maximum value. Once the maximum traction is reached, the interface starts failing and the traction reduces to zero up as the displacement increases up to a critical value according to the traction-displacement relationship. The propagation of a crack can thus be simulated as the consecutive failure of interface elements. These cohesive laws are often called “*initially elastic*” laws and they can have different shapes, such as exponential [2], trapezoidal [4] and bi-linear [5,6].

In the extrinsic approach, interface elements are introduced in the mesh only after the corresponding interface is predicted to start failing. Beginning the calculation with a regular mesh, the stress acting along the interface between two volumetric elements is monitored at any time to evaluate where crack will initiate. Once the stress reaches a critical value, a zero-thickness interface element is inserted by duplicating the nodes. Unlike the initially elastic interface elements, the initial cohesive response is rigid and the initial cohesive traction is equal to the critical stress [3]. Then, the interface opens in accordance with a prescribed traction-separation relation called “*initially rigid*” cohesive law.

Recently, Falk et al. [1] have demonstrated that the prediction of crack branching strongly depends on whether the initially rigid or initially elastic approach is used. The reason why the initially rigid approach showed absence of crack branching is unclear. The purpose of this work is to study this issue using a bi-linear initially elastic cohesive law where the initial stiffness is varied from low to high values without affecting the maximum cohesive traction or the cohesive energy. In this way, the initially elastic model is approached asymptotically to the initially rigid and, therefore, a detailed analysis of the material behavior can be carried out.

2. Approach used by M. Falk, A. Needleman and J. Rice[1]

In [1], Falk and co-workers compare the extrinsic approach proposed by Camacho and Ortiz [5] with the intrinsic approach proposed by Xu and Needleman [2]. As explained in [3], using the extrinsic approach, new fracture surfaces are created by splitting nodes according to a brittle fracture criterion. In quadratic triangular elements, mid-side nodes can only be split in one way, namely along the unique element boundary crossing that node. By contrast, interior corner nodes

can potentially open up along multiple fracture paths, all of which need to be evaluated in turn. To this end, Camacho and Ortiz [3] begin the process by computing the traction \mathbf{t} acting at the node across all potential fracture surfaces. If this traction satisfies the fracture criterion, the nodes involved in that surface are split in order to create two new surfaces. The details of the computation are given in [3]. As previously mentioned, this kind of interface element is called “*initially rigid*” cohesive element.

For the intrinsic approach, potential cohesive surfaces are introduced along all boundaries in a finite element mesh where cracks may initiate and propagate. When these “*initially elastic*” cohesive surfaces are introduced along all finite element boundaries, the mechanical response clearly depends on the mesh spacing, as well as on physical parameters. In fact, the exponential formulation proposed by Needleman has the feature that the cohesive surfaces contribute to the linear elastic response of the body. For example, the normal traction of this law is given by the following expression:

$$T_n = T_{\max} \left(\frac{u_n}{\delta_{\max}} \right) \exp \left(1 - \frac{u_n}{\delta_{\max}} - \frac{u_t^2}{\delta_{\max}^2} \right) \quad (1)$$

where T_{\max} is the maximum cohesive strength, u_n is the normal displacement, u_t is the tangential displacement and δ_{\max} is the maximum separation. The initial stiffness (or spring constant in this law) will be given by $\mathbf{k} = T_{\max} e / \delta_0$, which is fixed by a given cohesive energy G_{Ic} and maximum strength T_{\max} . As explained in the next section, when all the finite element boundaries are taken to be cohesive surfaces, the cohesive contribution to the overall stiffness has to be small compared to that of the volumetric constitutive relation. If h is the mesh spacing (or element size), then the following inequality should be satisfied

$$T_{\max} e / \delta_{\max} \gg E / h \quad (2)$$

On the other hand, the length of the cohesive element has to be small enough to resolve the cohesive zone length. This cohesive zone length l_{cz} is a measure of the length over which the cohesive constitutive relation plays a role. In the cohesive law proposed by Needleman [1,2] the cohesive element length should satisfy the following expression:

$$h \ll l_{cz} \approx \frac{\pi}{2} \left(\frac{E}{1-\nu^2} \right) \frac{G_{Ic}}{T_{\max}} \quad (3)$$

As shown in [1], conditions (2) and (3) cannot be satisfied simultaneously; consequently it is not possible to resolve the cohesive zone without affecting the compliance of the solid. In order to overcome this difficulty, Falk and co-workers have been forced to introduce an independent distance between cohesive surfaces, l_c . In other words, the cohesive interfaces have not been included in every element boundary. Instead, they have been placed with a distance l_c between each other, independently of h . It should be noted that the numerical simulations presented in their work, have been obtained using two different codes [1].

3. Approach used in this work

The results presented in this report have been obtained using the finite element code FEAP, originally written by Zienkiewicz and Taylor [7] and modified later by Espinosa and co-workers [8-10]. FEAP is an explicit finite element program for structural/continuum mechanics problems. Due to its explicit nature, it is especially efficient to solve transient dynamic problems. Six-node quadratic triangular continuum elements and four-node zero thickness interface cohesive elements are used. A detailed description of the material continuum models, contact algorithms and other features of this code can be found in previous works [8-10].

In the present work, the technique used for the automatic insertion of interface elements in the 6-node triangular mesh is similar to that given in [11]. Figure 1(a) shows the interface elements embedded between the six-node triangular elements. Figure 1(b) shows a typical calculation showing crack propagation and branching following the element boundaries.

3.1 Cohesive law

The bi-linear cohesive law [5, 6] is proposed for this analysis. The normal and tangential tractions are given by the following expressions:

$$T_n = \frac{1-\lambda}{\lambda} \left(\frac{u_n}{\delta_n} \right) \frac{T_{\max}}{\lambda_{cr}} \quad \text{and} \quad T_t = \frac{1-\lambda}{\lambda} \left(\frac{u_t}{\delta_t} \right) \frac{\alpha T_{\max}}{\lambda_{cr}} \quad (4)$$

where $\alpha = \beta^2 \left(\frac{\delta_n}{\delta_t} \right)$ and $\lambda = \sqrt{\left(\frac{u_n}{\delta_n} \right)^2 + \beta^2 \left(\frac{u_t}{\delta_t} \right)^2}$ is monotonically increasing and it has the form $\lambda = \max \left(\lambda_{\max}, \lambda \right)$.

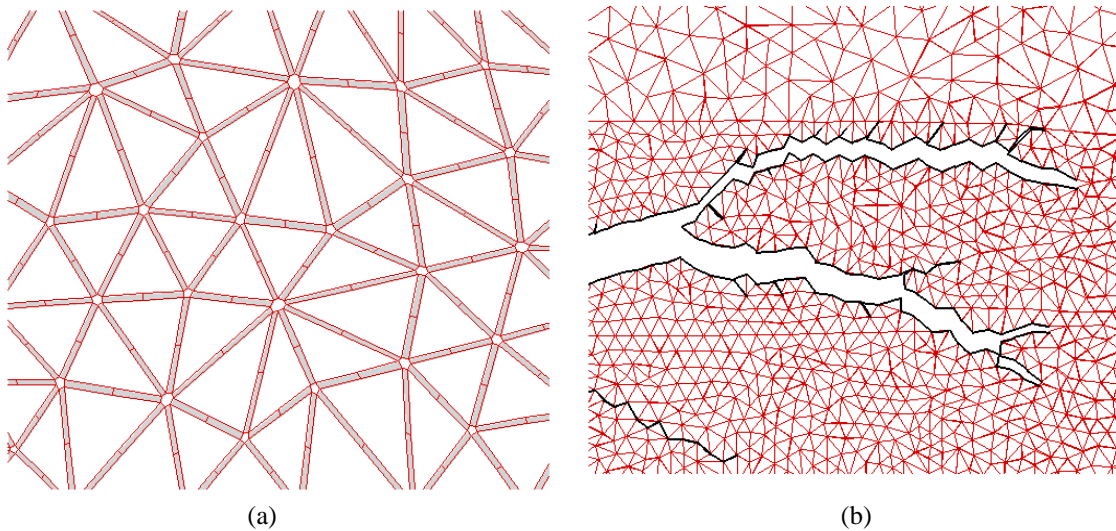


Figure 1: (a) Finite element mesh used with embedded “zero-thickness” cohesive elements. The continuum elements were shrunk for illustration purposes. (b) Typical calculation showing the crack evolution, the black solid lines indicate the creation of the new surfaces as the interface elements fail.

3.1.1 Initially elastic cohesive approach: Equation (4) describes an initially elastic cohesive law. The traction across the cohesive surface is a continuous function of the displacement jump that starts from zero when the displacement jump is zero and increases monotonically up to a critical value. Due to the finite stiffness at small values of the displacement jump across the cohesive surface (when $u / \delta_{max} < \lambda_{cr}$), the stiffness of the cohesive surfaces contributes to the linear elastic response of the solid.

3.1.2 Initially rigid cohesive approach: The implementation in a finite element code of the initially rigid cohesive element, such as the one discussed in Section 2, requires adaptive insertion of new interface elements, node duplication and intensive bookkeeping. A possible workaround can be developed to use the bi-linear cohesive law of Eq. (4) with $\lambda_{cr} = 0$ and the same pre-inserted interface elements, but this time, without allowing the nodes to move independently. We refer to those nodes as being “*tied*” (See Figure 2(a)). Each set of tied nodes is regularly checked to determine if they can be released according to a fracture criterion. If the criterion is satisfied, the interface element is activated and the nodes can move according to Eq. (4) and $\lambda_{cr} = 0$ (Figure 2(b)). The implementation of this technique implies the identification of the nodes with same original coordinates. Interface elements are only active to check the fracture condition. The stresses from the Gauss point of the quadratic triangular elements are extrapolated to the nodes connected to the interface elements (See Figure 2(a)). The contribution of the stress in those nodes is translated into normal and tangential tractions (T_n and T_t) using the local system of coordinates of the interface elements. If these tractions satisfied the fracture criterion $\sqrt{T_n^2 + \beta^2 T_t^2} \geq T_{max}$ the nodes are released and the cohesive interface element is activated, otherwise the nodes on both potential surfaces of the interface elements are “*tied*” following the standards procedures to do so. The development of this technique in the code FEAP is still an on going work.

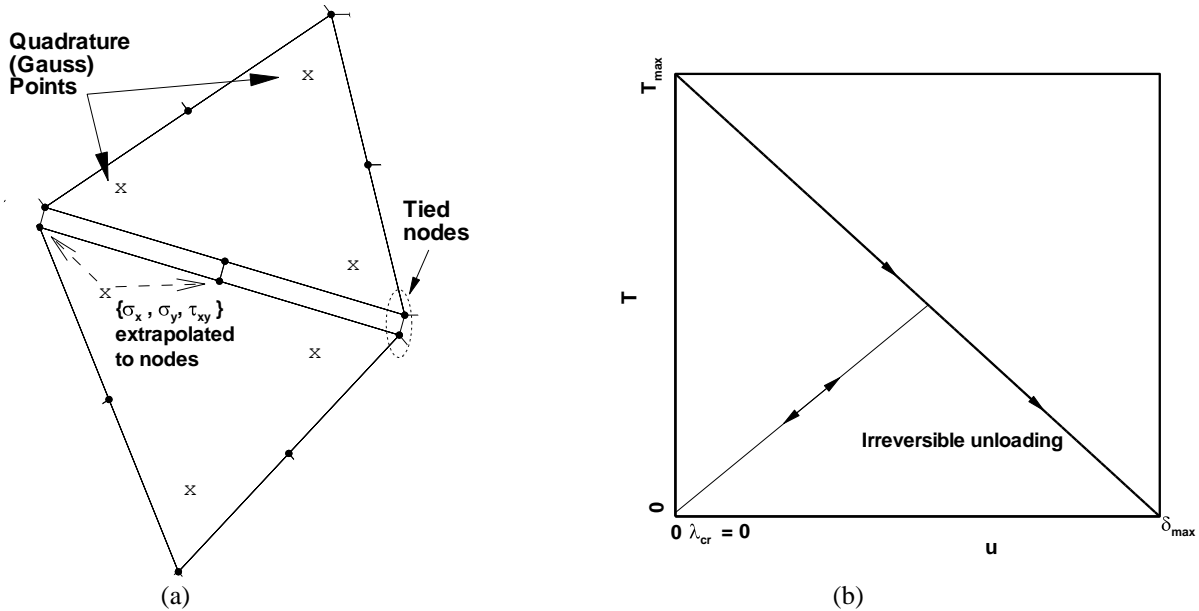


Figure 2: (a) Two 6-node elements with “*tied*” nodes. Once the normal and tangential traction in those nodes reach a critical value the nodes are “*released*”. (b) Cohesive law given by Eq. (4) when $\lambda_{cr} = 0$.

A second alternative proposed in this work is to approach initially rigid cohesive model by making $\lambda_{cr} \rightarrow 0$ in Equation (4). As explained later in Section 4.1, the initial stiffness \mathbf{k} is increased up to the limit $\mathbf{k} \rightarrow \infty$, (as $\lambda_{cr} \rightarrow 0$). In practice, λ_{cr} can only be decreased until a certain value before the calculation becomes computational intensive and numerical instabilities are significant [10].

3.2 Initial elastic stiffness

A competing requirement when initially elastic cohesive surfaces are embedded between volumetric elements is that the cohesive contribution should not affect the elastic compliance of the material. According to the traction-separation relation ($T - u$) of the constitutive cohesive law considering only normal separation, the initial stiffness is given by

$$\mathbf{k} = T_{\max} / (\lambda_{cr} \delta_{\max}) \quad (5)$$

where T_{\max} is the maximum cohesive strength, δ_{\max} is the maximum separation and λ_{cr} is the critical displacement jump such that the interface fails when the opening displacement $u \geq \lambda_{cr} \delta_{\max}$. Figure 3(a) shows the curve $T - u$ represented in the non-dimensional axis T/T_{\max} and u/δ_{\max} . The value of λ_{cr} should be selected such that the elastic response of the material with interfaces is the same as that of the material without interfaces during reversible loading (when $u \leq \lambda_{cr} \delta_{\max}$ and $T \leq T_{\max}$). From the numerical point of view this stiffness works as a penalty parameter. It has to be large enough to be effective but not so large as to provoke numerical instabilities.

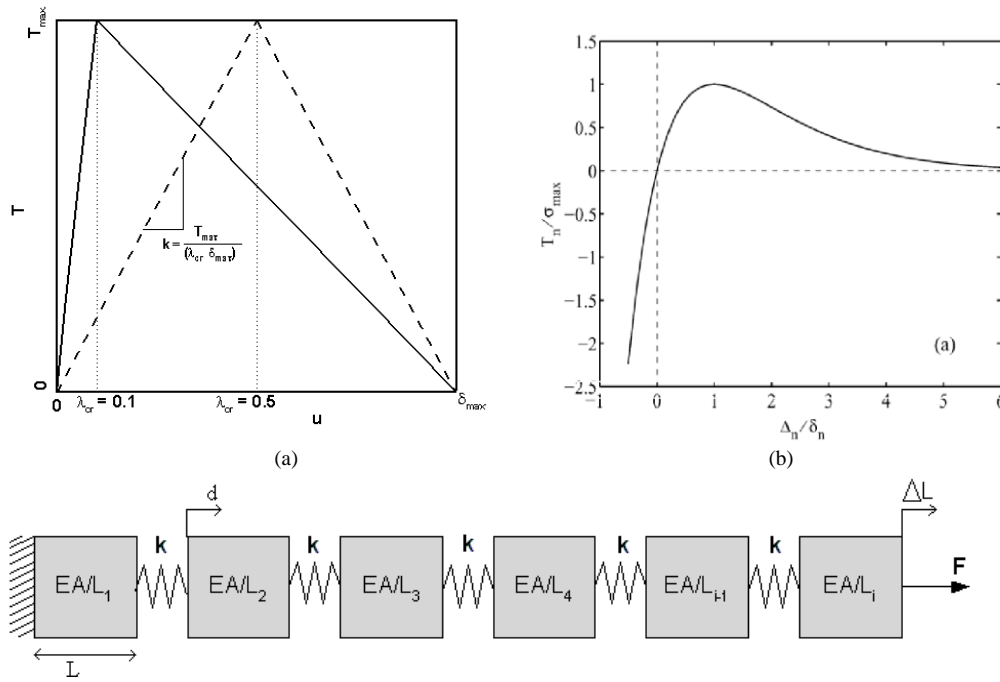


Figure 3: (a) Traction-separation law in 1-D showing the initial stiffness \mathbf{k} . The maximum traction takes place when $(u/\delta_{\max}) = \lambda_{cr}$, where λ_{cr} can take any value from 0 to 1. (b) Needleman's law for the normal traction. The maximum traction is located at $\lambda_{cr} = \tau_n / \delta_{\max} = 1$. (c) Schematics of the one-dimensional block connected with linear springs. The spring stiffness should be larger than the Young's modulus of the material such that the overall stiffness is not affected by the presence of the springs

In order to obtain a theoretical estimate of the right initial stiffness, a very simple example is considered. A 1-D block is subjected to simple force \mathbf{F} on one of its sides and constrained on the other (See Figure 3(c)). The block is divided in N sub-blocks of length L_i connected by springs of the same stiffness. Analogous to the 2D case, springs work as cohesive elements during the first linear stage ($u \leq \lambda_{cr} \delta_{max}$). Therefore, the response of material with “linear” springs should be the same as the one of the block without springs. Let $\Delta L_i = (L_i \mathbf{F} / EA)$ be the deformation of each individual block and $d = (\mathbf{F} / \mathbf{k}A)$ the separation between them given by the stiffness of the springs (Note: For this example \mathbf{k} represents the stiffness per unit area A such that it can be compared with Equation (5)). Assuming that all the sub-blocks have the same length, area and Young’s modulus and the springs the same stiffness, the total displacement at the right end of the block is given by

$$\Delta L = \sum_N \left(\frac{L_i}{EA} \right) \mathbf{F} + \sum_N \left(\frac{1}{\mathbf{k}A} \right) \mathbf{F} = \left(\frac{NL_i}{EA} + \frac{N}{\mathbf{k}A} \right) \mathbf{F} \quad (6)$$

The separation given by the springs should be much smaller than the elastic deformation of the material, such that $\Delta L = \left(\mathbf{F} / EA \right)$. Then

$$\frac{NL_i}{EA} \gg \frac{N}{\mathbf{k}A} \quad (7)$$

If each sub-block is considered to be a finite element of length h , then the following inequality should be satisfied

$$\mathbf{k} \gg E/h \quad (8)$$

Unlike Needleman’s formulation, the bi-linear cohesive law is “flexible” in the sense that the initial stiffness can be changed without affecting the physical parameters. The critical displacement jump λ_{cr} can vary from 0 to 1 independently of T_{max} or δ_{max} . Figure 3(a) shows the traction-displacement law represented in the axis T and u for two different values of λ_{cr} . On the other hand, the initial stiffness of the exponential law (given by $\mathbf{k} = T_{max} e / \delta_0$) can only be modified with T_{max} or/and δ_{max} . It should be mentioned that the maximum traction in the exponential law takes place at $\lambda_{cr} = \left(\mathbf{k}_n / \delta_{max} \right) \delta_0 = 1$.

4. Case Study: Crack growth on a pre-cracked block

A pre-cracked block is utilized for these analyses as shown in Figure 4. Plane strain conditions are assumed to prevail and a Cartesian coordinate system is used as reference with origin at the initial crack tip position. The length of the specimen is L and the width is $2W$. The block is loaded in uni-axial tension with zero shear traction at the top and bottom boundaries. The tensile axis is aligned with the y -direction and a crack of initial length $2a_0$ lies along the line $y=0$. In our example $L = W = 3 \text{ mm}$ and $a_0 = 0.25 \text{ mm}$. The side boundaries are stress free. The initial condition is defined by uniformly applied velocity gradients in the x - and y -directions with strain rates $\dot{\epsilon}_{yy} = 2000 \text{ s}^{-1}$ and $\dot{\epsilon}_{xx} = 0$.

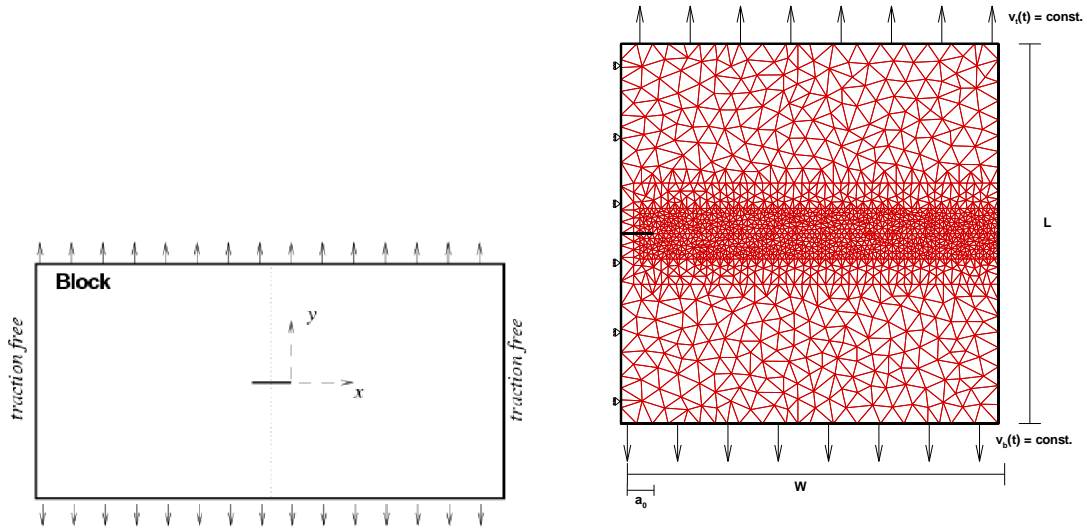


Figure 4: Schematics of the geometry considered in this analysis.

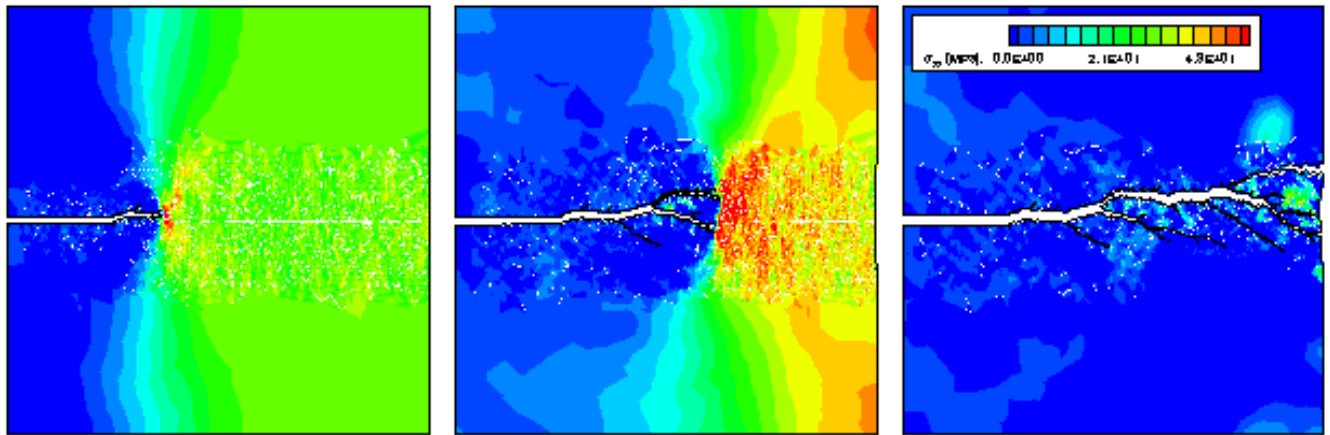


Figure 5: Evolution of the tensile stress σ_{yy} at different times during the propagation and branching of the initial crack. The black solid lines indicate the creation of the new surfaces as the interface elements fail. Dispersion of the contours is artificially caused by the stresses of the nodes connected to interface elements.

The velocities at the top and bottom boundaries are not altered during the simulation (these velocities are $v_y = \pm 3 \text{ m/s}$). This loading does not generate waves propagating in from the top and bottom boundaries, although these boundaries will reflect waves generated by the propagating crack tip. Symmetry at $x = -0.25 \text{ mm}$ requires the displacement to be $u_x = 0$. The free surface of the initial crack remains traction free. In this analysis, cohesive interface elements are only embedded in the region indicated in Figure 4.

Following the analysis of Needleman and co-workers [1,2], the elastic constants consistent with PMMA have been chosen: $E = 3.24 \text{ GPa}$, $\nu = 0.35$ and $\rho = 1190 \text{ kg/m}^3$. This results in dilatational, shear and Rayleigh wave speeds of $c_d = 2090 \text{ m/s}$, $c_s = 1004 \text{ m/s}$ and $c_r = 938 \text{ m/s}$. Following Falk et al. [1], the cohesive parameters used for this analysis are: $T_{max} = E/25 = 129.6 \text{ MPa}$, $\delta_n = \delta_t = \delta_{max} = 3 \mu\text{m}$. For these values the l_{cz} , given by Equation (3) is $l_{cz} = 67 \mu\text{m}$. Therefore a mesh with an element size of $h = 20 \mu\text{m}$ near the initial crack plane and $h = 0.1 \text{ mm}$ at the top and bottom boundaries

has been chosen. The finite element mesh used for this analysis is shown in Figure 4. The box indicates the region where the cohesive interface elements were included. Note that this is a non-structured mesh generated in such way that symmetry was not respected. However, element boundaries lay on the original crack plane ($y = 0$) so the crack is not inhibited of growing straight if conditions are given. All these parameters, including the boundary conditions, are kept constant unless otherwise indicated. In Figure 5, the evolution of the tensile stress σ_{yy} when the crack propagates from side to side and branches in the middle can be seen. The “*broken*” interface elements (with $\lambda \geq 1$) are plotted with a black line indicating the shape and length of the crack at any given moment.

4.1 Analysis of the variation of the initial stiffness \mathbf{k}

An analysis of the variation of the initial stiffness \mathbf{k} was carried out. Values of \mathbf{k} and λ_{cr} for this analysis are tabulated in Table 1. For this specific material and mesh size, \mathbf{k} should be much higher than $E/h = 0.162 \text{ GPa}/\mu\text{m}$. The objective is to determine how large this cohesive stiffness has to be with respect to the material stiffness in order to achieve convergence. In other words, we can define the non-dimensional parameter ξ as the ratio between the cohesive stiffness and the material stiffness such as $\mathbf{k} = \xi \cdot (E/h)$. Consequently, the condition in Eq. (8) becomes $\xi \gg 1$.

$\mathbf{k} [\text{GPa}/\mu\text{m}]$	$\xi = \mathbf{k}/(E/h)$	λ_{cr}
0.04	0.25	0.9
0.08	0.50	0.5
0.43	2.65	0.1
0.54	3.33	0.08
0.86	5.31	0.05
4.32	26.67	0.01
10.80	66.67	0.004
86.40	533.34	0.0005

Table 1: Initial stiffness \mathbf{k} and ratio ξ (for $E/h = 0.162 \text{ GPa}/\mu\text{m}$).

Starting from a very low initial stiffness $\xi = 0.25$ ($\mathbf{k} = 0.04 \text{ GPa}/\mu\text{m}$), the calculations have been carried out to analyze the behavior of the crack evolution as a function of the initial stiffness up to $\xi = 533.34$ (See Table 1). All the simulations have been carried out until 15 microseconds. The same boundary and loading conditions are applied for all the cases. Material and cohesive parameters are the same except for the critical effective displacement jump λ_{cr} that controls the initial stiffness. The crack evolution at different times is plotted in Figure 6 for all the eight cases presented in Table 1. The two cases with initial stiffness lower than the material stiffness ($\xi < 1$) are presented in Figure 6(a) and (b). The crack evolution is plotted from the 6 to 14 μsec (with 1 μsec between frames). Although both cases show crack branching, the crack pattern and time of crack growth initiation are different. In the case with $\xi = 0.25$, the crack growth initiation occurs at about 8 μsec and crack branching at 10 μsec , whereas in the second case $\xi = 0.50$ the crack starts to growth at 6 μsec and crack branching at 9 μsec . It should be observed that, although the

problem is symmetric, the crack pattern is not symmetric in any of these cases. This is essentially caused by the lack of symmetry of the non-structured mesh.

Figures 6(c)-(h) show the rest of the calculations for $\xi > 1$. These plots only show the evolution up to 11 μsec because the crack reaches the right side of the block in less time. Although crack branching occurs in all the cases, large branches are more evident for lower values of ξ , especially for the cases in which the cohesive stiffness is comparable with the bulk stiffness. It can be observed from Figure 6(c) that the case with $\xi = 2.65$ shows three significant branches. On the other hand, the cases with $\xi = 3.33$ and $\xi = 5.31$ (Figure 6(d) and (e), respectively), develop side branches of short length. The only peculiarity about them is that one of the branches grows longer and then changes its direction to the perpendicular to the crack plane.

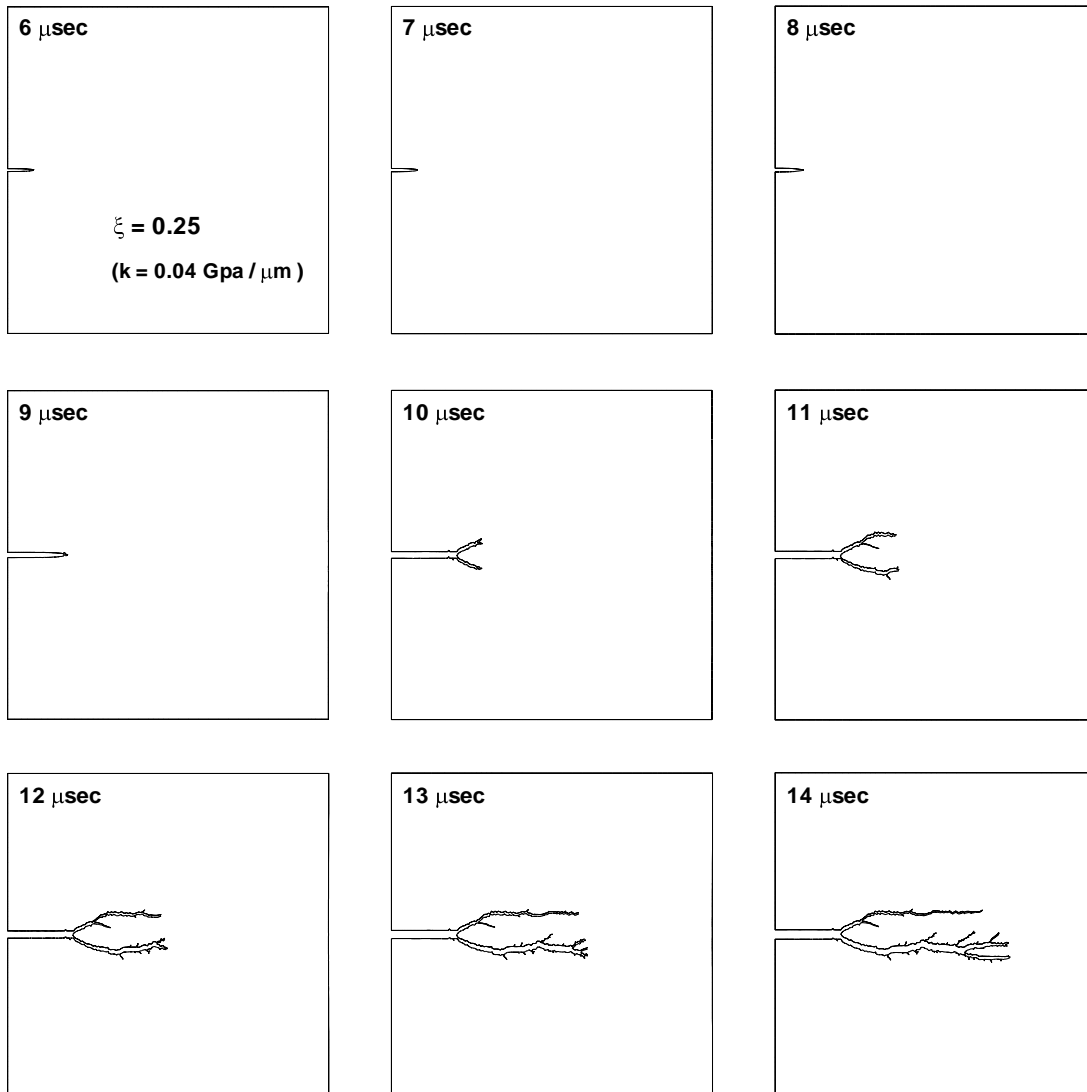


Figure 6 (a): Crack evolution for $\xi = 0.25$.

The cases with $\xi \gg 1$ are illustrated in Figures 6(f), (g) and (h). It is evident from these plots that crack patterns are similar in all the cases. The case with highest stiffness $\mathbf{k} = 533.34$ shows some crack branching at the end of the block. However, instabilities after that point were found and the run was stop before $10 \mu\text{sec}$, therefore it is concluded that the cohesive stiffness is too high for the current element size and time step.

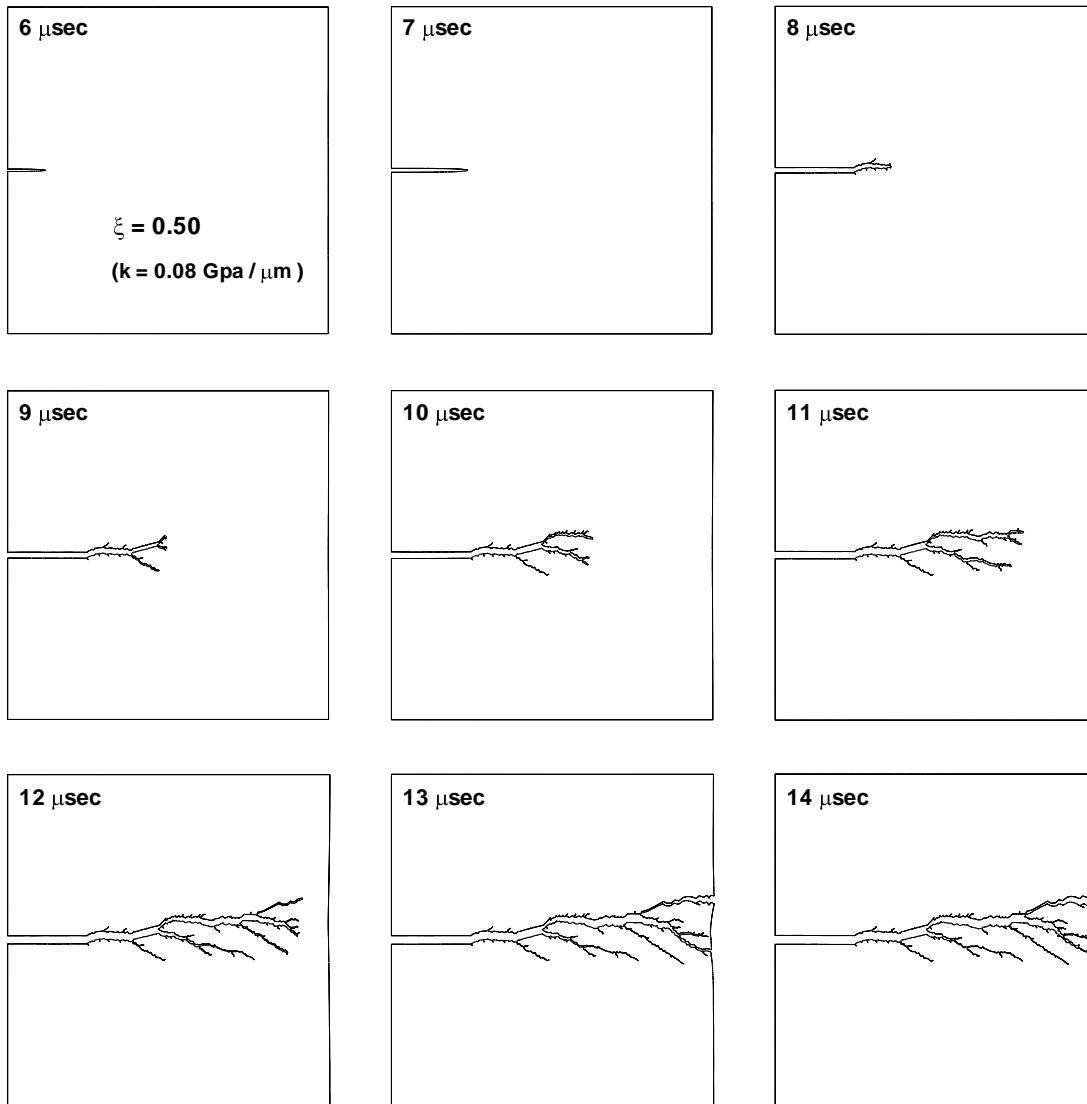


Figure 6 (b): Crack evolution for $\xi = 0.50$

We can conclude that for low ξ (or low initial stiffness) crack branching is more significant and crack speed seems to be slowed down. As explained by Needleman [1,2], a drop on the crack speed can be seen as the energy spent to create these new surfaces. Although some branching is observed for the cases with $\xi \gg 1$, the crack grows from side to side in less time. As mentioned before, it is evident that convergence is achieved for the cases with $\xi \geq 26.67$. For these cases, the lateral branches develop from the main crack with similar angles as those reported by Yu et al. [12] for

similar strain rates. Hence, it can be said that when the initial stiffness \mathbf{k} satisfies the condition of Eq. (6) the crack behaves in a similar manner and the response of the initially elastic cohesive surfaces approaches the response of the initially rigid cohesive surfaces represented here as $\xi \gg 1$.

The only shortcoming is the calculation time when the initial stiffness is significantly high. As previously reported by Zavattieri et al. [10], time step is reduced considerably for higher values of the cohesive stiffness. Therefore, cases with $\xi > 500$ may require very small time steps. However, it is demonstrated here that values of $\xi \approx 10 - 100$ give similar results.

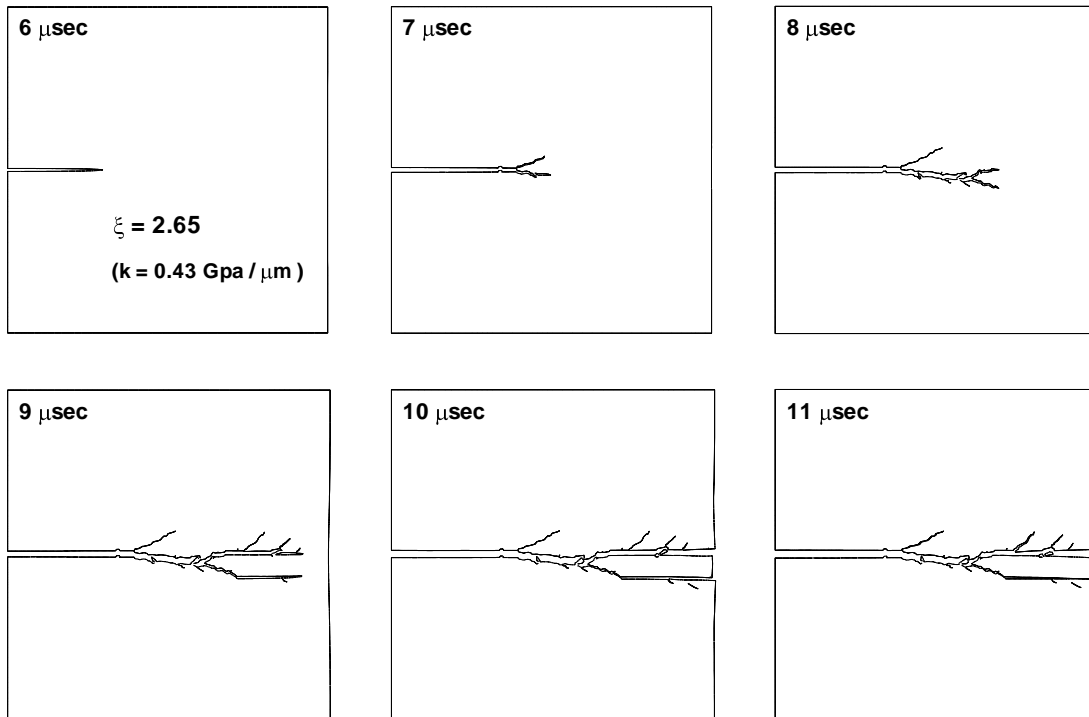


Figure 6 (c): Crack evolution for $\xi = 2.65$

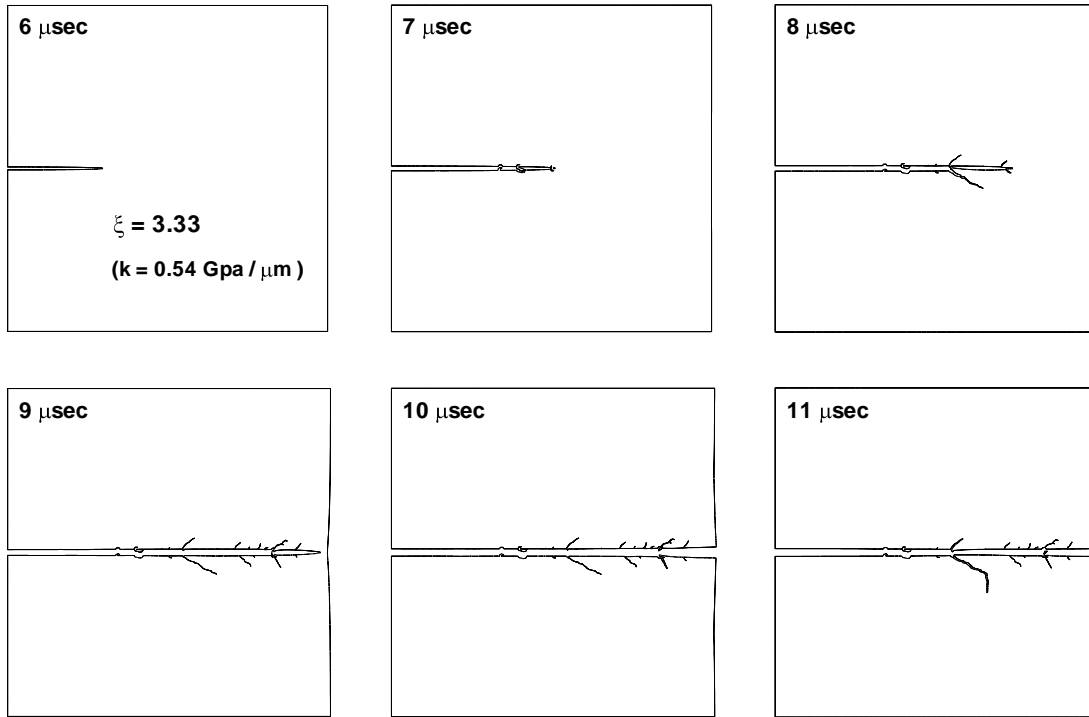


Figure 6 (d): Crack evolution for $\xi = 3.33$

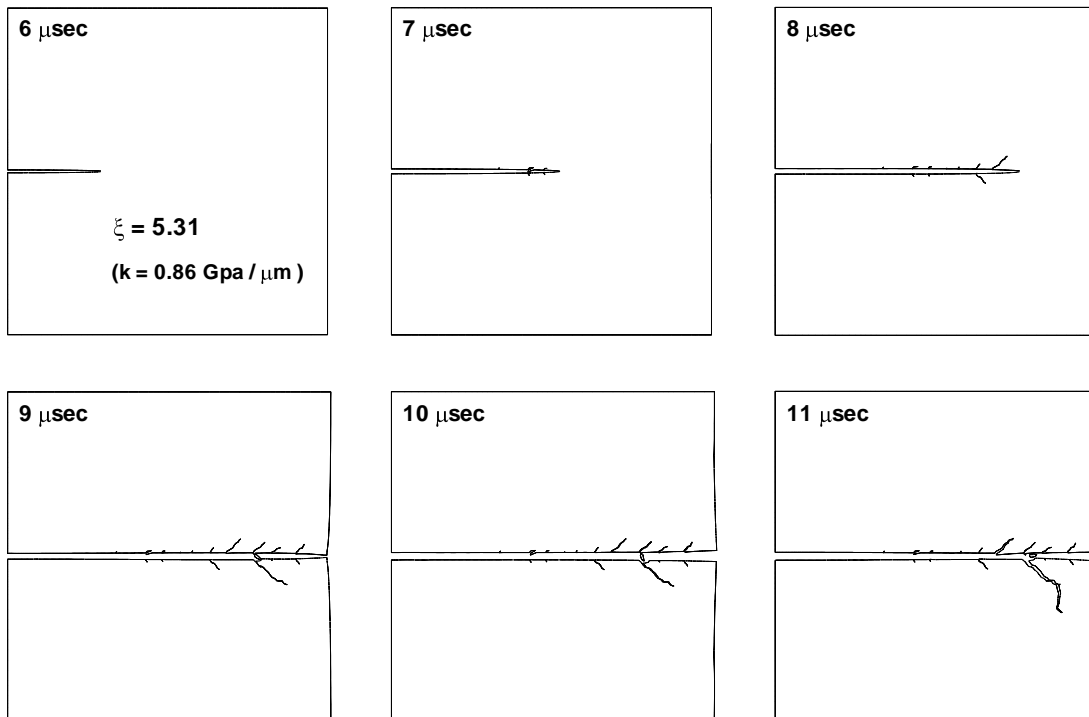


Figure 6 (e): Crack evolution for $\xi = 5.31$

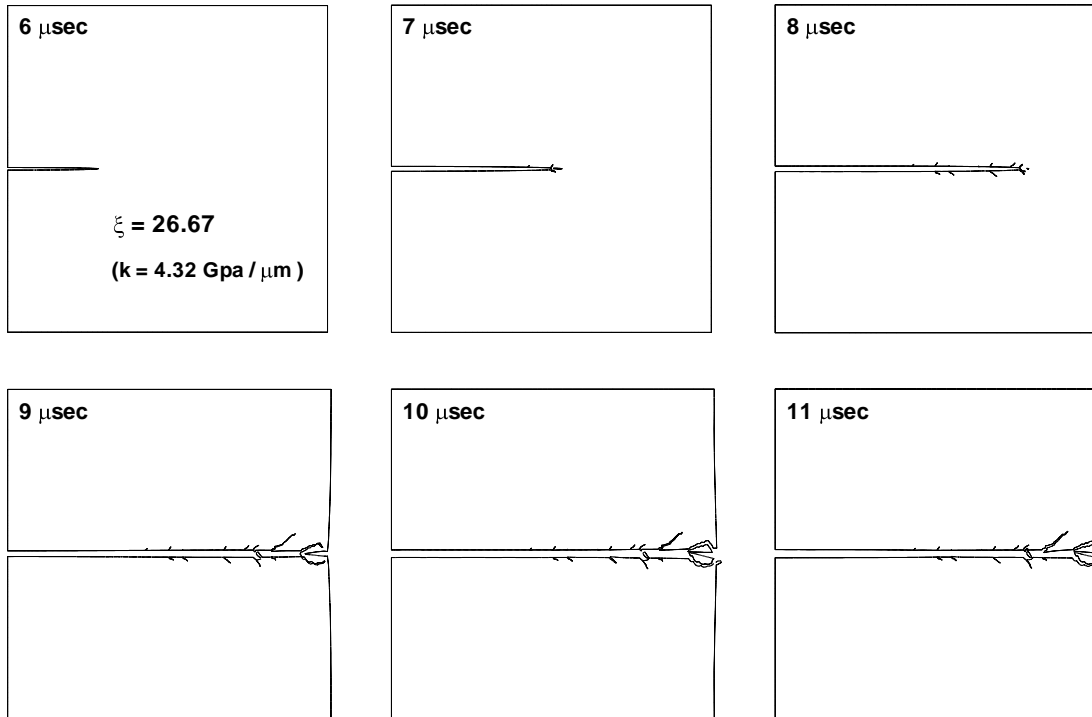


Figure 6 (f): Crack evolution for $\xi = 26.67$

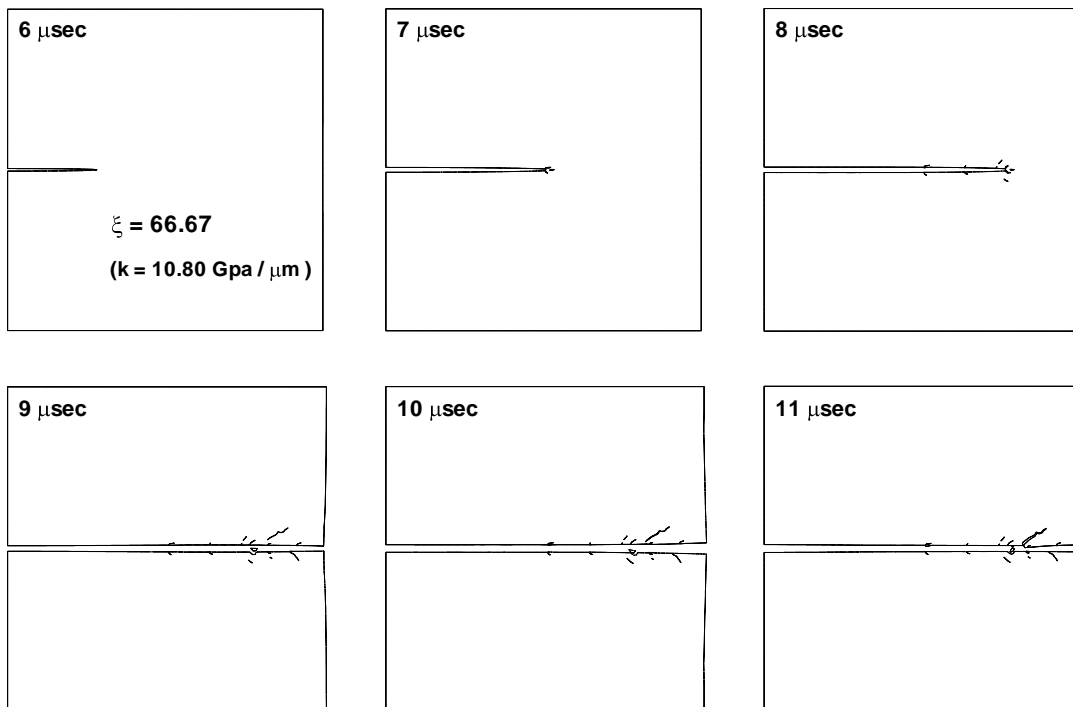


Figure 6 (g): Crack evolution for $\xi = 66.67$

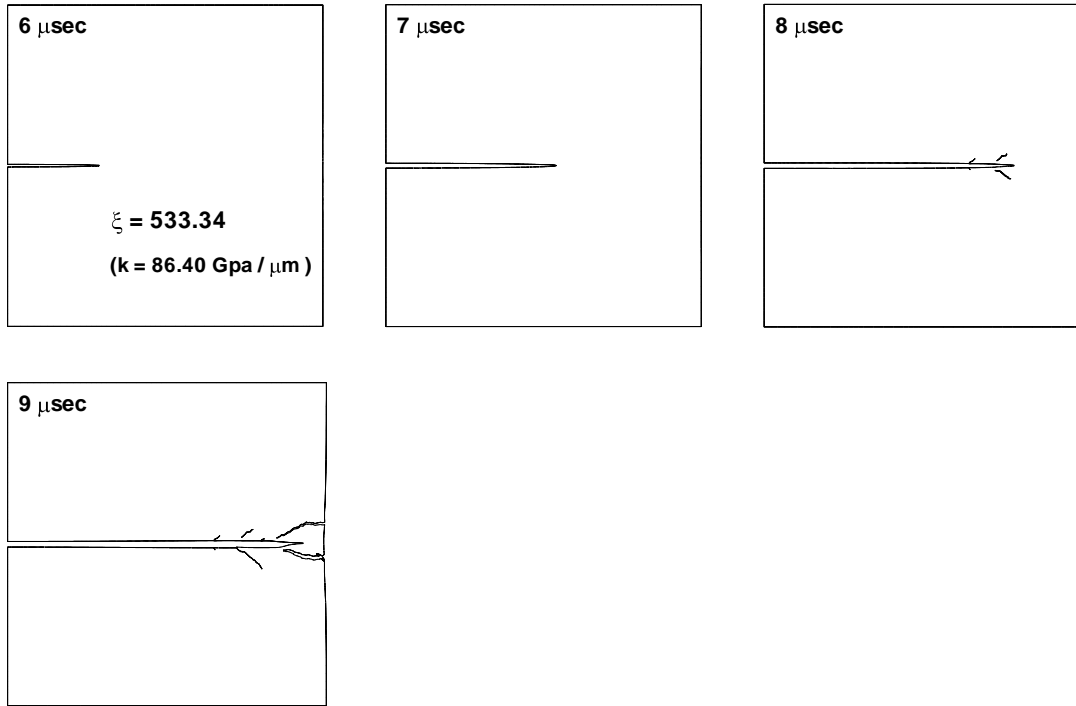


Figure 6 (h): Crack evolution for $\xi = 533.34$

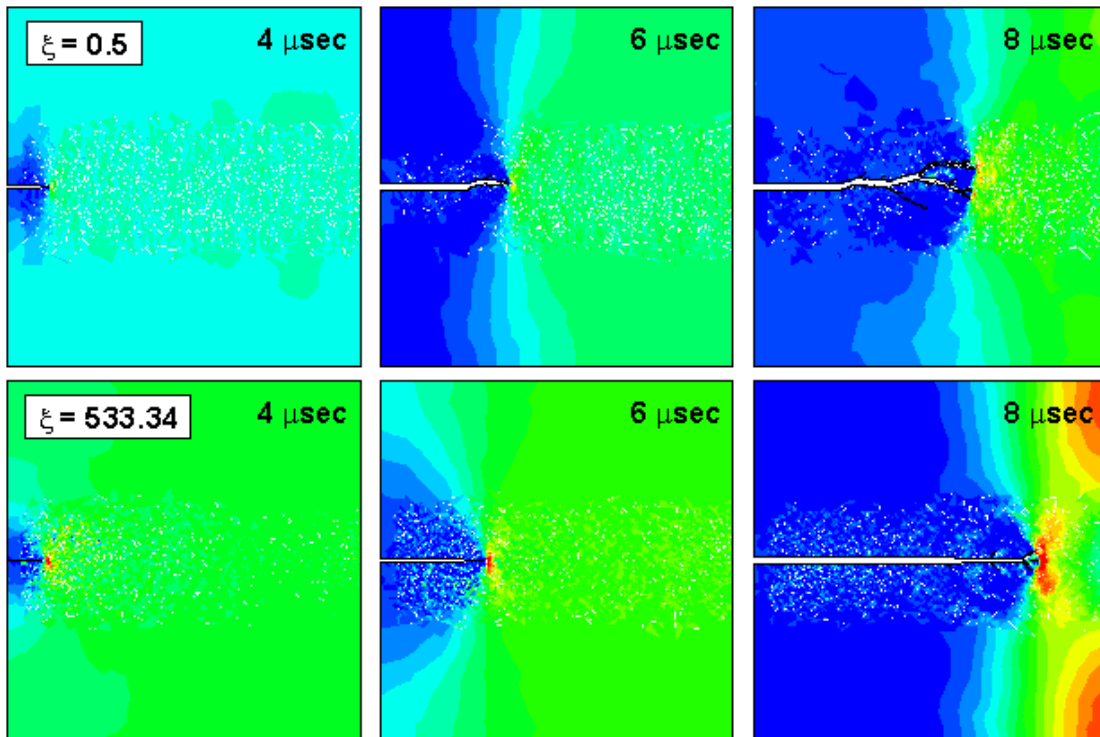


Figure 7: Crack and stress evolution for two extreme cases: $\xi = 0.5$ and 533.34 .

Figure 7 shows the evolution of the crack pattern and stress σ_{yy} for two extreme cases, $\xi = 0.5$ and 533.34. Dispersion of the contours is artificially caused by the stresses of the nodes connected to interface elements. In addition to the observation previously discussed, the stress concentration is more evident for the case with less branching (higher ξ).

The evaluation of the normal and tangential cohesive tractions given by Eq. (4) takes place at the two Gauss points of the four-node interface element [2-6]. Once the displacement jump is equal to the unity, the part of the element corresponding to that Gauss point is considered broken. Once that condition is reached in both Gauss points, the whole element is “broken”. In Figures 6 and 7, the broken elements are plotted with a black line indicating the shape and length of the crack at any moment. If the projection on the x -axis of the Gauss points is stored at the time when the condition $\lambda \geq 1$ is satisfied, one can plot the crack tip position as a function of time, except that, when there is branching, one or more crack tips can exist at the same time. Figure 8 (a) shows the projection of the crack tip position on the x -axis for low values of ξ . As previously observed, the crack tip speed is appreciably slower for those cases with low ξ , while crack branching becomes more important. Figure 8(b) shows the crack tip position as a function of time for $\xi \gg 1$. For these cases, the crack pattern is similar and secondary cracks are much shorter.

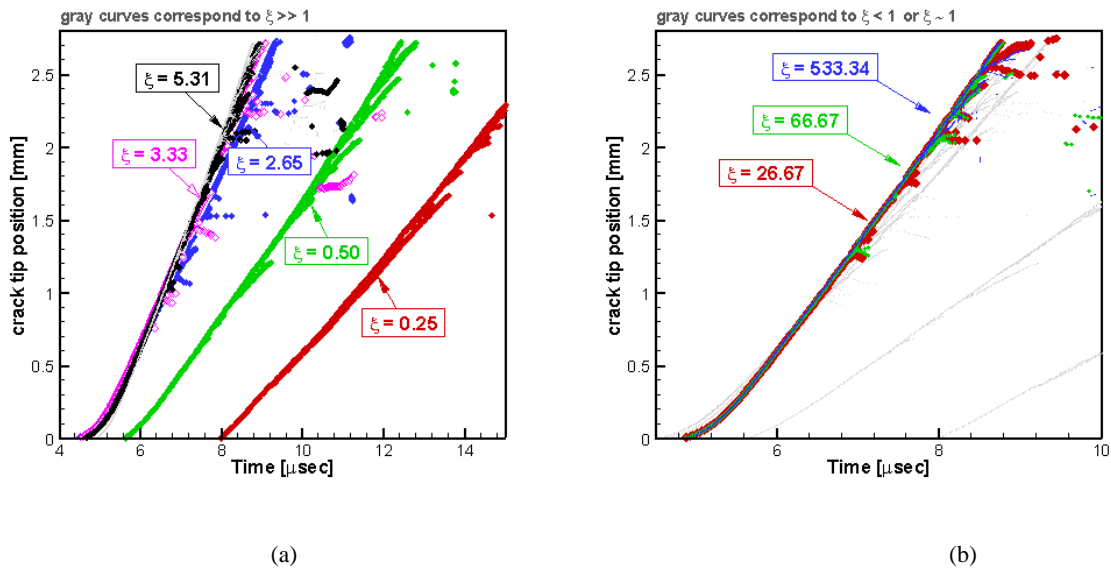


Figure 8: (a) Crack evolution for low values of ξ . Crack initiation delayed and branching is more significant when $\xi \leq 1$. (b) Simulations with $\xi \gg 1$ show similar results.

Another characteristic attributed to the initial cohesive stiffness is that the time and position of the crack tip where branching occurs are different in each case. Figure 9 shows the time and position of the crack tip when branching occurs for different values of ξ . The initiation time for the first three branches is plotted in Figure 9(a). When $\xi \gg 1$, the crack seems to branch earlier than for the cases with lower values of ξ . On the other hand, the position of the crack tip when branching takes place increases with ξ . As observed in Figures 6-8, the crack tip speed is delayed low values of ξ , therefore crack branching is also delayed and takes place closer to the original crack tip position than for the cases with $\xi \gg 1$.

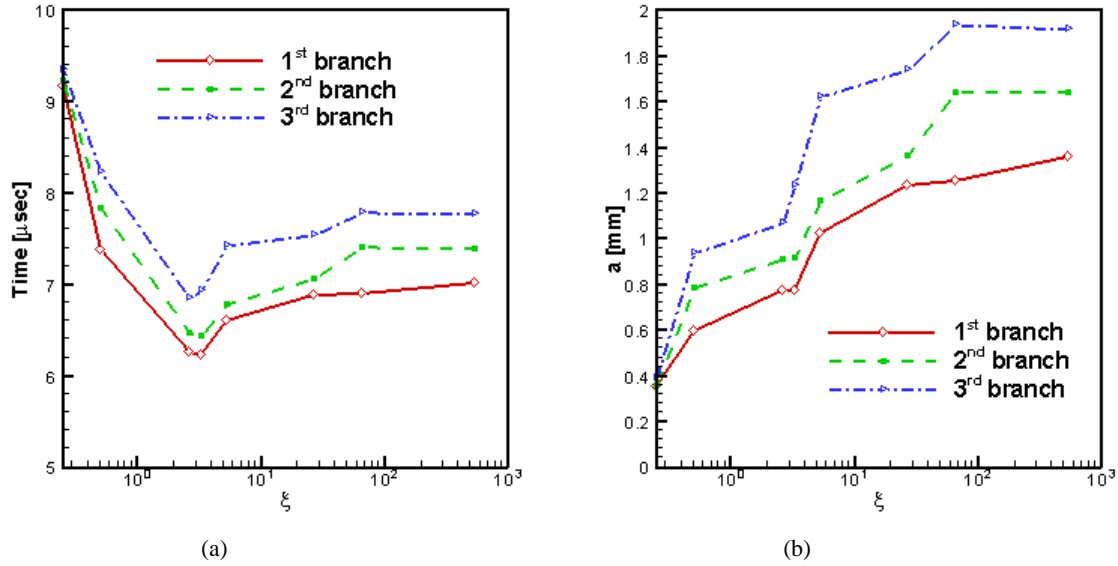


Figure 9: (a) Time when branching occurs for different values of ξ . Solid line represents the first time when crack branching occurs, the dashed line the second branching and so on. (b) Projection on the x -axis of the crack position where crack branching occurs.

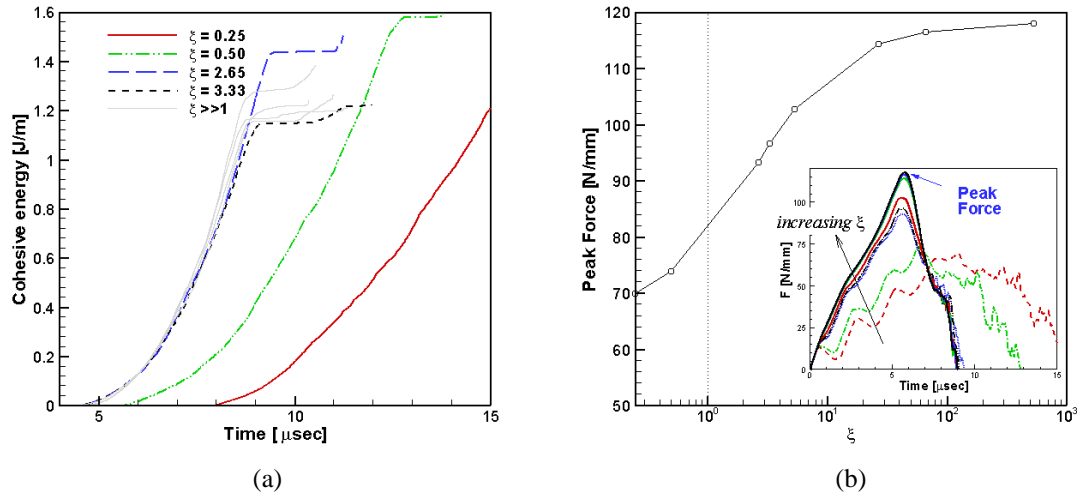


Figure 10: (a) Cohesive energy dissipated during the process of propagation and branching (b) Force vs time and Maximum force at the top boundary as a function of ξ . The vertical dotted line indicates $\xi = 1$.

It is evident from Figures 6 to 9 that condition (8) ensures convergence of the analysis. However, only crack patterns, times and position have been compared so far. The energy absorbed by material separation can be easily computed by integrating the dissipated cohesive energy along the interface elements. Figure 10(a) shows the evolution of the cohesive energy as a function of time for different values of ξ . The cases with $\xi \gg 1$ have been plotted with the same color indicating that they almost lead to the same result. On the other hand, the total force per unit thickness at the top and bottom boundaries was also recorded during the calculation and plotted in Figure 10(b). It is perceived that the maximum peak load and the time where it occurs are drastically affected for low values of ξ . Even the overall shape of the force-time curve changes radically for $\xi < 1$. Therefore, it can be

concluded that the peak force can vary, as much as 40% if the right initial stiffness is not used.

4.2 Analysis with other values of T_{max} and δ_{max}

The behavior of the crack evolution when other values of T_{max} and δ_{max} are used has been analyzed in this section. The main idea is to verify if the behavior of the crack as a function of the initial cohesive stiffness observed in previous cases is also observed with different cohesive parameters are used. For this analysis, the cohesive parameters used in Section 4.1 will be given as a reference case (i.e., $T_{max}^0 = E/25 = 129.6 \text{ MPa}$, $\delta_n = \delta_t = \delta_{max}^0 = 3 \mu\text{m}$). In addition, two more pairs T_{max} , δ_{max} are considered. Case 1: $T_{max} = T_{max}^0/2$ and $\delta_{max} = 2\delta_{max}^0$. Case 2: $T_{max} = T_{max}^0$, $\delta_{max} = 2\delta_{max}^0$. Figure 11 shows the comparison between these three different cohesive laws. The idea is to compare the behavior of the crack for two extreme values of the initial stiffness: $\mathbf{k} = 0.04$ (or $\xi = 0.25$) and $\mathbf{k} = 10.8 \text{ GPa} / \mu\text{m}$ (or $\xi = 66.67$) for each of these different sets of cohesive parameters.

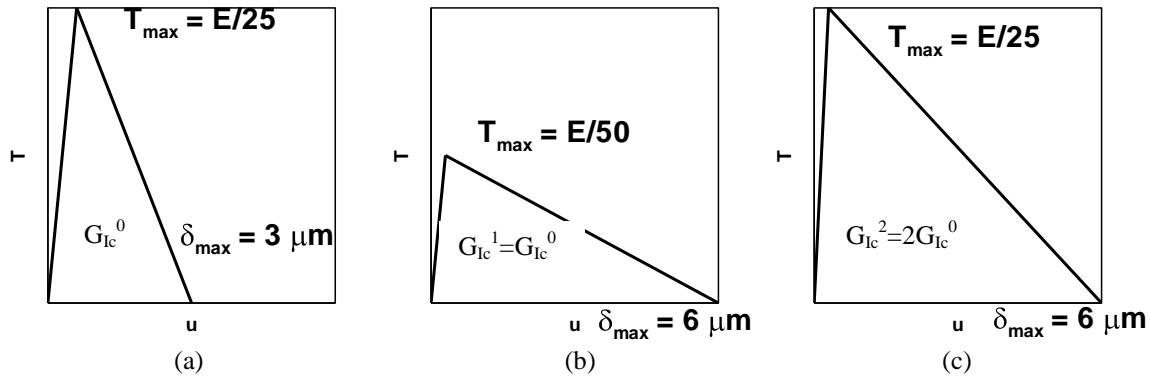
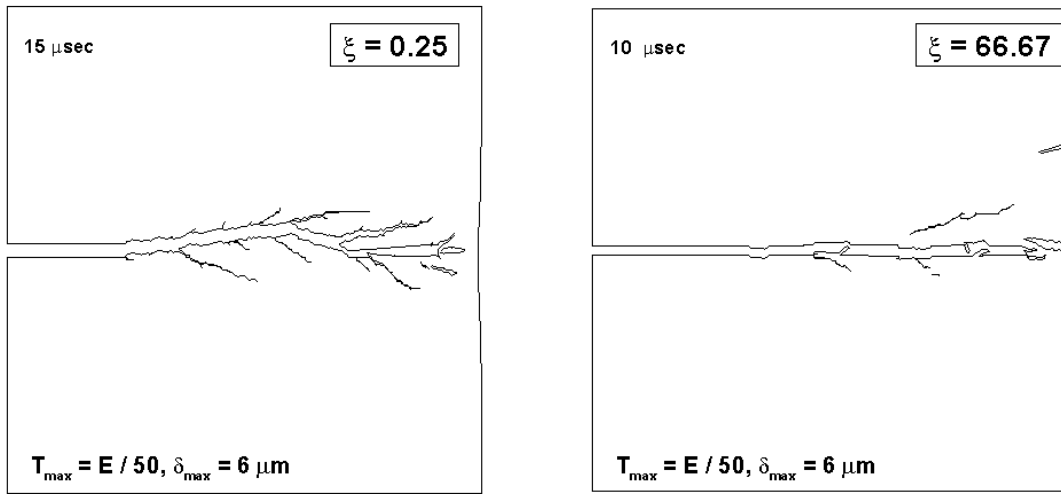


Figure 11: Traction-separation law for different values of T_{max} , δ_{max} and same initial stiffness \mathbf{k} (a) Reference case: Cohesive parameters used in Section 4.1 (T_{max}^0 , δ_{max}^0) (b) Case 1: $T_{max} = T_{max}^0/2$ and $\delta_{max} = 2\delta_{max}^0$. (c) Case 2: $T_{max} = T_{max}^0$ and $\delta_{max} = 2\delta_{max}^0$.

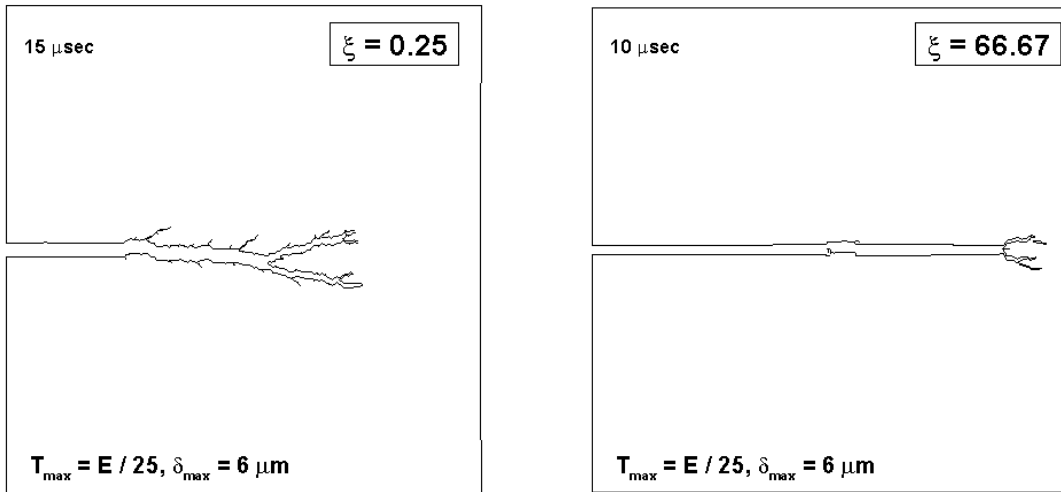
Figure 12 shows the crack pattern for Case 1 ($T_{max} = E/50$ and $\delta_{max} = 6 \mu\text{m}$) using $\xi = 0.25$ (Fig. 12(a)) and $\xi = 66.67$ (Fig. 11(b)) at the time the crack tip reaches the other end of the plate. These cohesive parameters are such that the cohesive energy is the same as the analyzed in the previous section. Comparing these results with the ones shown in Figure 6(a) and (b), we can observe that the crack evolution is similar. Although the initial stiffness is the same, λ_{cr} is different for each case (See Table 1). This means that the crack behavior is likely to be controlled by the initial stiffness of the cohesive surfaces and not by the critical displacement jump λ_{cr} , which is a non-physical parameter. Figures 13 (a) and (b) show the crack pattern for case 2 with $T_{max} = E/50$ and $\delta_{max} = 6 \mu\text{m}$. (a) $\xi = 0.25$ (b) $\xi = 66.67$.



(a)

(b)

Figure 12: Case1: $T_{max} = E/50$ and $\delta_{max} = 6 \mu m$. (a) $\xi = 0.25$ (b) $\xi = 66.67$. Compare with Figure 6(a) and (e)



(a)

(b)

Figure 13: Case 2: $T_{max} = E/25$ and $\delta_{max} = 6 \mu m$. (a) $\xi = 0.25$ (b) $\xi = 66.67$.

5. Summary

In this report, an analysis where the intrinsic method is approached asymptotically to the extrinsic method was presented. The calculations reported here show that simulations of crack branching with initially elastic and initially rigid cohesive elements can lead to different results. As reported by Falk et al. [1], the initially rigid cohesive elements do not alter the elastic response of the material but they inhibit crack branching. In their work, they showed simulations with two different codes; the calculations with initially rigid interfaces have been performed by Ortiz and co-workers while the calculations with initially elastic interfaces have been performed using Needleman's code

(See figure 14). Prof. M. Ortiz mentioned that the fact that no branching was present in his calculation was due to an error in his code [14]. However, recent reports [12], show that the implementation issue was circumvented.

The main problem of the cohesive law proposed by Needleman is that the initial stiffness could not be changed. In order to circumvent this problem, they introduced an additional length scale into the problem such that the element could be smaller than the cohesive zone length and at the same time the material stiffness was not affected by the presence of interface elements. In other words, they limited the number of interface elements in the mesh, such that the distance between them (given by l_c) was such that $\mathbf{k} \gg E/l_c$. The main limitation of this technique is that the number of potential crack paths was limited by l_c instead of the element size (which is much less than l_c).

Unlike the exponential formulation proposed by Needleman, the bi-linear cohesive law used in this work allows the conditions of Equations (2) and (3) to be satisfied simultaneously. This means that the analyst can choose the element size to be as small as it is necessary to properly capture the cohesive zone length and enrich the number of potential crack paths and at the same time select λ_{cr} such that $\mathbf{k} = f(T_{max}, \delta_{max}, \lambda_{cr}) \gg E/h$.

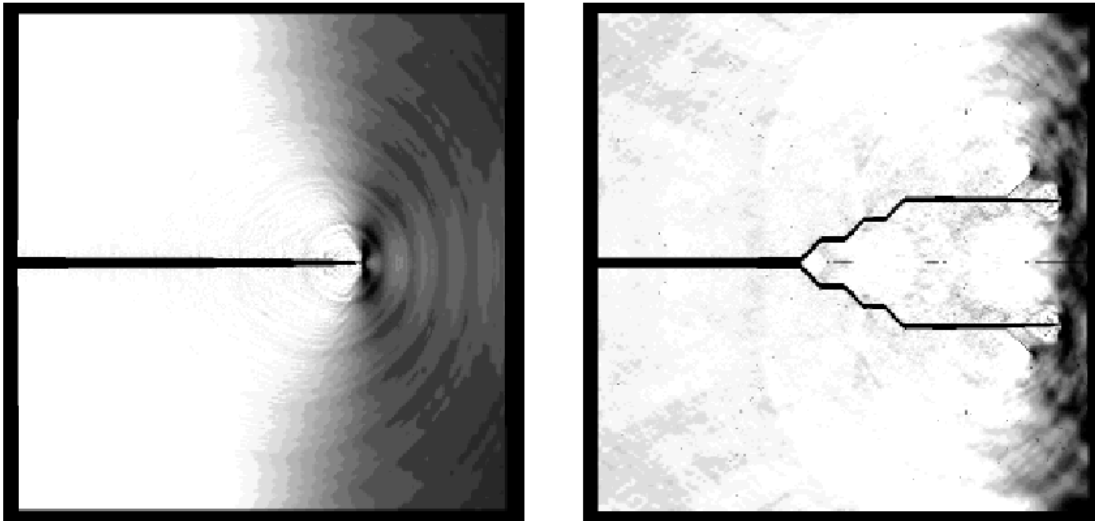


Figure 14: Results shown by Falk, Needleman and Rice [1] for the extrinsic approach (left: initially rigid cohesive law) and the intrinsic approach (right: initially elastic cohesive law). The gray scale denotes the local σ_{yy} -stress. The crack does not undergo any macroscopic branching in the initially rigid case while in the initially elastic case the crack bifurcates and travels off axis by many times the cohesive zone length.

The main characteristics observed in the calculation included in this report can be summarized in the following way:

- (a) When the initial stiffness \mathbf{k} of the cohesive surfaces has the same order of magnitude or less than the material stiffness, crack branching becomes more significant and crack tip speed decreases.
- (b) Similar crack patterns are observed for cases where the initial stiffness is significantly higher than the material.

- (c) The time and position of the crack tip where branching occurs are different when $\xi < 1$. However a trend is observed when $\xi \gg 1$.
- (d) Maximum peak force is also affected by the stiffness of the cohesive elements.

As a general comment we can mention that as long as the initial stiffness of the cohesive interfaces is such that the material stiffness is not affected, the intrinsic and extrinsic approach lead to the same results. Whether or not one technique is more expensive, from the computational point of view, will depend on the material and fracture properties. If ξ is a very high number (such that $k \gg E/h$) the intrinsic approach could result in a very intensive calculation due to fact that the time step has to be small. In that case, the extrinsic approach, using the technique given in Section 3, could be a solution. In general, the intrinsic approach (with initially elastic cohesive interfaces) is much easier to implement than the extrinsic approach. However, for several materials, a reasonable value for λ_{cr} can be always found such that the stiffness of the material is not affected.

Recently Kubair and Geubelle [15] addressed the same problem with regards to the fundamental problem of the steady-state and transient mode III crack propagation.

6. Acknowledgments

The author would like to thank Prof. Marcos Actis and the *Departamento de Aeronautica* of *Universidad Nacional de La Plata* for their support during his stay in Argentina. The author also acknowledges Prof. Horacio Espinosa from *Northwestern University* for providing the source code of the finite element code FEAP, which has been partially developed by the author during his Ph.D. work.

References

- [1] M. Falk, A. Needleman, J. Rice, "A critical evaluation of dynamic fracture simulations using cohesive surfaces", 5th European Mechanics of Materials Conference, Delft, The Netherlands, March 5-9, 2001.
- [2] X.-P. Xu and A. Needleman "Numerical simulations of fast crack growth in brittle solids", *J. Mech. Phys. Solids*, 42(9), pp. 1397-1434, 1994.
- [3] G. Camacho and M. Ortiz, "Computational modeling of impact damage in brittle materials", *Int. J. Solids Structures*, 33, pp. 2899-2938, 1996.
- [4] V. Tvergaard and J. W. Hutchinson, "The relation between crack growth resistance and fracture process parameters in elastic-plastic solids", *J. Mech. Phys. Solids*, **40**, pp. 1377-1397, 1992.
- [5] P.H. Geubelle and J. Baylor, "Impact-induced delamination of laminated composites: a 2D simulation", *Composites B*, **29**, pp. 589-602, 1998.
- [6] P.D. Zavattieri and H.D. Espinosa, "Grain level analysis of ceramic microstructures subjected to normal impact loading", *Acta Materialia*, 49(20), pp. 4291-4311, 2001.

- [7] Zienkiewicz O.C. and Taylor R.L. "The Finite Element Method. 2", Mc Graw Hill, fourth edition, 1991.
- [8] Espinosa H.D., Zavattieri P.D. and Emore G.L. "Adaptive FEM computation of geometric and material nonlinearities with application to brittle failure", *Mechanics of Materials*, 29 pp. 275-305, 1998.
- [9] Espinosa H.D., Zavattieri P.D. and Dwivedi S., "A finite deformation continuum/discrete model for the description of fragmentation and damage in brittle materials", *J. Mech. Phys. Solids*, 46(10), pp. 1909-1942, 1998.
- [10] P.D. Zavattieri, P.V. Raghuram and H.D. Espinosa, "A computational model of ceramic microstructures subjected to multi-axial dynamic loading *J. Mech. Phys. Solids*, 39(1), pp. 27-68, 2001.
- [11] Zavattieri P.D., "Cohesive interface elements for 3D shell and hexahedral elements. Part II: Pre-processor for Dyna3D", research report submitted for publication.
- [12] Yu C., Pandolfi A. and Ortiz M. "3D cohesive investigation on branching for brittle materials", *International Conference on Fracture and Damage Mechanics*, Milan, Italy, 2001.
- [13] Sharon E., Fineberg J. "Universal features of the microbranching instability in dynamic fracture", *Philos. Mag.* 78(2). Pp. 243-251, 1998.
- [14] Ortiz M, Discussion in one of the session of the 6th U.S. Congress on Computational Mechanics to be held in Dearborn, MI in August, 2001.
- [15] D. V. Kubair, P.H. Geubelle, "Comparative analysis of extrinsic and intrinsic cohesive models of dynamic fracture", *Int. J. Solids Structures*, **40**(15), pp. 3853-3868, 2003.